Journal of Physics: Materials

OPEN ACCESS

RECEIVED
27 March 2026

REVISED
22 May 2026

ACCEPTED FOR PUBLICATION
3 July 2026

PUBLISHED
17 July 2026

PAPER

Tailoring defect-driven ferroelectric topologies in $Bi_6Ti_{2.8}Fe_{1.52}Mn_{0.68}O_{18}$ via vicinal-substrate growth

Louise Colfer[1], Michele Shelly Conroy[2], Núria Bagués[3,4,5], David McComb[3,4], Jonathan Alaria[6,7], Michael Schmidt[1], Roger W. Whatmore[2,8] and Lynette Keeney[1,*]

[1] Tyndall National Institute, University College Cork, Lee Maltings Complex, Dyke Parade, Cork T12 R5CP, Ireland
[2] Department of Materials, Faculty of Engineering, Imperial College London, London SW7 2AZ, United Kingdom
[3] Center for Electron Microscopy and Analysis, The Ohio State University, Columbus, OH 43212, United States of America
[4] Department of Materials Sciences and Engineering, The Ohio State University, Columbus, OH 43210, United States of America
[5] Alba Synchrotron Source Light Facility, CELLS, Cerdanyola del Vallès, Barcelona, Spain
[6] Department of Physics, University of Liverpool, Oxford Street, Liverpool L69 7ZE, United Kingdom
[7] Leverhulme Centre for Functional Materials Design, The Materials Innovation Factory, University of Liverpool, 51 Oxford Street, Liverpool L7 3NY, United Kingdom
[8] School of Chemistry, University College Cork, Cork, Ireland
[*] Author to whom any correspondence should be addressed.

E-mail: lynette.keeney@tyndall.ie

Keywords: multiferroics, ferroelectric, Aurivillius phases, defects, charged domain walls, polar vortices

Supplementary material for this article is available online

Abstract

Room-temperature multiferroics such as Aurivillius-phase $Bi_6Ti_{2.8}Fe_{1.52}Mn_{0.68}O_{18}$ (B6TFMO, $m = 5$) combine ferroelectricity and ferrimagnetism, making them promising for next-generation memory and spintronic devices that exploit domain walls and magnetoelectric coupling. Naturally occurring defects, including out-of-phase boundaries (OPBs), stacking faults, and 'anatase'-type intergrowths, profoundly influence local strain, electrostatics, and magnetic cation ordering, enabling charged domain walls, polar vortices, and enhanced magnetic interactions. However, their uncontrolled distribution undermines reproducibility across films. Here, we introduce vicinal sapphire substrates (0.2° to 10° miscut) as a powerful handle for engineering these defects during direct liquid injection chemical vapour deposition growth. Systematic increases in step density drive proliferation of OPB defects and stacking faults, along with grain refinement and x-ray diffraction peak broadening/asymmetry, while also triggering tilted (∼10°) *b*-axis polarisation vectors that enhance vertical polarisation accessibility. Atomic-resolution scanning transmission electron microscopy reveals OPB defects serving as heterogeneous nucleation sites for 180° nominally charged domain walls and polarisation patterns consistent with polar vortices (stabilised 3–5 nm apart). Nanorod precipitates within 'anatase'-type interlayers stabilise novel anti-hedgehog polarisation configurations reminiscent of skyrmion-like topologies in Aurivillius phases. Critically, PFM uncovers a three-fold reduction in out-of-plane switching voltage (±5 V) for high-miscut films, enabled by selective *c*-axis response: ∼10° tilted grains rotate the in-plane *b*-axis polarisation vertical, while defect networks pin lateral domains and channel domain wall motion driven by local strain/electrostatic energy gradients. These findings establish substrate vicinality as a reproducible strategy to sculpt defect landscapes and directionally tune ferroelectric switching in Aurivillius multiferroics, paving the way for sustainable, low-voltage, scalable nanoelectronics with designer polar topologies.

1. Introduction

Room temperature (RT) multiferroics with coupled ferroelectricity and ferromagnetism have exciting applications in future memory storage technologies such as domain wall [1–3] and magnetoelectric spin orbit logic devices [4, 5]. Aurivillius phase $Bi_6Ti_{2.8}Fe_{1.52}Mn_{0.68}O_{18}$ (B6TFMO) is a rare example of a RT

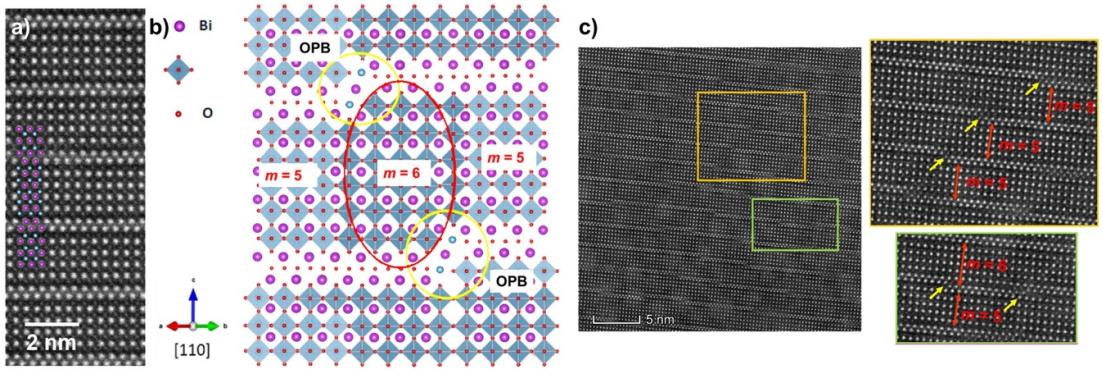

Figure 1. (a) HAADF-STEM image of defect-free B6TFMO viewed along the [110] zone axis, showing the characteristic layering of the Aurivillius structure. Purple spheres represent Bi^{3+} cations (A-sites) within the fluorite layers; blue spheres indicate B-site transition metal cations at octahedral centres. (b) Schematic illustration of the Aurivillius layered structure showing OPB defects (within yellow circles) and an $m = 6$ stacking-fault intergrowth (within red circle). The structure comprises alternating $[Bi_2O_2]^{2+}$ fluorite layers and perovskite ABO_3 blocks, with Bi^{3+} occupying A-sites and transition metals occupying B-sites. (c) Left: HAADF-STEM (high-angle annular dark-field scanning transmission electron microscopy) image of a B6TFMO thin film showing OPB defects and associated stacking faults. Right: Enlarged HAADF-STEM images of regions marked by orange and green rectangles in the middle image, highlighting OPB defects (yellow arrows) propagating through the film and frequently associated with $m = 6$ stacking-fault intergrowths in a film grown on a 0.5° miscut sapphire substrate.

magnetoelectric multiferroic. It is orthorhombic with lattice parameters of *a*, *b*, and *c* of 0. 5497, 0. 5415, and 4. 9280 nm, respectively [6]. The material has previously been synthesised by both chemical solution deposition [6] and direct liquid injection chemical vapour deposition (DLI-CVD) [7] on *c*-plane sapphire substrates miscut by 0.2 ° toward the *m*-plane $(10\bar{1}0)$. A miscut vicinal substrate is a single crystal substrate intentionally cut slightly off-axis from a major low-index crystallographic plane (e.g. *c*-plane sapphire cut slightly toward *m*-plane), producing a regular array of atomic-scale steps and terraces.

Aurivillius phase systems are naturally layered structures having a general formula $(Bi_2O_2)(A_{m-1}B_mO_{3m+1})$, where dielectric bismuth oxide $(Bi_2O_2)^{2+}$ fluorite-type layers are interleaved with *m* numbers of ferroelectric perovskite-type units. B6TFMO is an example of one such layered system where $m = 5$. B6TFMO is very tolerant of non-stoichiometry and the $m = 5$ phase has been fabricated with compositions ranging from $Bi_6Ti_{2.3}Fe_{1.95}Mn_{0.75}O_{18}$ to $Bi_6Ti_{2.8}Fe_{1.52}Mn_{0.68}O_{18}$ with the *c*-axis lattice parameter varying from 4. 855 nm to 4. 929 nm respectively for these compositions [8].

The large unit cell and inherent structural flexibility of the Aurivillius phase enables B6TFMO to sustain robust ferroelectricity through stereochemically active Bi^{3+} $6s^2$ lone-pair electrons and Ti–O covalency arising from hybridisation between the Ti^{4+} 3d and O 2p orbitals, while simultaneously accommodating magnetic cations such as Mn and Fe. However, this structural adaptability also makes the films susceptible to the formation of structural defects. As with other layered materials having high structural anisotropies such as the Ruddlesden-Popper [9], Dion-Jacobson [10, 11] and layered cuprate phases [12], out-of-phase boundary (OPB) defects, intergrowths and stacking faults are a common occurrence and can significantly impact material properties in thin films [13, 14].

OPB defects are defined as defects created when a fraction of the unit cell in a material is displaced in the *c*-axis direction between two neighbouring regions (figure 1). Anti-phase boundary (APB) defects are a special case of OPB defects when this displacement is 0.5 unit cells in the *c*-axis direction. These defects, which form during thin film synthesis, appear as 'steps' when viewed edge-on and can significantly influence the properties of the materials [15–20]. They often nucleate at the substrate-film interface and can then propagate up through the entire thin film, accompanied by perturbations to the crystal lattice, inducing local strain fields and non-uniform electrostatics.

Stacking faults (figure 1) are two-dimensional planar defects. They occur in crystal systems when there is a deviation in the regular stacking sequence of the crystal planes [21]. In a perfect crystal, the stacking sequence within a material remains constant through the entire crystal, however when the sequence is disrupted, a stacking fault can form. Stacking faults can occur in a material during crystal growth, as part of other defects within the structure (e.g. partial dislocations) or they can evolve from other defects (such as from the result of an OPB defect). A common type of stacking fault observed in Aurivillius phase materials is the addition or subtraction of a perovskite unit cell between the $[Bi_2O_2]^{2+}$ layers at an OPB defect, thus leading to regions where *m* changes by ± 1, or potentially more than 1, where stacking faults are considered as intergrowths of differing *m* numbers. Another type of intergrowth phase which has been observed in the B6TFMO system [22], is known as an 'anatase'-type

planar defect. This is a bismuth poor intergrowth in B6TFMO that appears where the $[Bi_2O_2]^{2+}$ layer usually resides. The 'anatase'- type planar defect is made up of chains of edge-sharing BO_6 octahedra and form 'S'-shaped tunnels, which contain *A*-cation columns. Where these defects occur in perovskite and Aurivillius systems, the 'S'-shape tunnels are stabilised by double columns of stereochemically active A-site cations with lone electron pairs e.g. Bi^{3+}.

Local elastic strain and electrostatic changes induced by structural defects have been observed to affect the physical properties within many material systems. At APB defects in $PbZrO_3$, the antiferroelectric arrangement of dipole moments is broken, with the new arrangement resulting in a local net ferroelectric behaviour at the APB defect [16]. These defects can also create favourable conditions for domain switching as observed in the $BiFeO_3$ system [15] and aid in the formation of ferroelectric domains. For example, when the Ruddlesden-Popper phase $Ca_{3-x}Sr_xTi_2O_7$ is substituted with Sr ions, there is an increase in the presence of OPB defects, which in turn increases the number of charged domain boundaries within the material [18]. In $Bi_{3.15}Nd_{0.85}Ti_3O_{12}$ (BNTO) Aurivillius phase films, OPB defects enhance in-plane B-site cation displacements while co-aligning their out-of-plane polarisation across perovskite layers [23]. In magnetic systems such as Fe_3O_4, the density of APB defects has been observed to have a negative impact on thin films. The strong antiferromagnetic interactions across the boundaries degrade the electronic and magnetic properties of the thin films [19, 20].

Recent studies on the B6TFMO system [24] have demonstrated that disruptions to the Aurivillius phase lattice by OPB defects and stacking-faults have a marked influence on the internal elastic strain and electrostatic energy gradients within the structure. While specific experimental studies on the effects of OPB defects on magnetic and magnetoelectric properties remain limited in multiferroic Aurivillius materials, these defects have a significant positive impact: they increase magnetic cation partitioning towards the central perovskite layer in B6TFMO, thereby facilitating elevated magnetic ion interactions [25]. Recent reviews establish that local magnetic structures, including domain walls, magnetic vortices, and other topological defects, exhibit intrinsic electric polarisation through flexomagnetoelectric coupling [26], whereby the enhanced magnetic cation ordering driven by OPB defects is expected to strengthen magnetoelectric coupling in B6TFMO. Furthermore, OPB defects facilitate the formation of extraordinary polarisation profiles such as nominally charged domain walls and polarisation patterns consistent with polar vortex domain wall-like topologies [24].

Since charged domain walls can be created, annihilated or moved on demand by applying simple voltage pulses, they are an emerging research focus in nano-electronics and domain wall devices. Owing to the highly anisotropic nature and strong electrostatic interactions in ferroelectrics, the characteristic length scales of polar topological structures are often much smaller (∼4–10 nm) than those in ferromagnets (∼10–100 nm). This makes them highly promising for ultra-high-density, energy-efficient memory devices [27–29]. In addition to energy-efficient data-storage capabilities, these recent discoveries of defect-driven polar topology formation [24] demonstrate the wider technological potential of multiferroic B6TFMO.

Fascinatingly, these topologies arise spontaneously in multiferroic B6TFMO, without the need for artificial interfaces or externally imposed strain. These layered materials therefore present us with the opportunity to grow materials with coupled ferroelectric and ferromagnetic properties mediated through their inherent defect-based topologies at a sub-10 nm length scale that is relevant to the highest densities of modern integrated circuits. There are very few studies of this in the literature. Gradauskaite *et al* [30]. and Yu *et al* [23]. have explored the link of OPB defects to the domain structure and polarisation in $Bi_5FeTi_3O_{15}$ (BFTO) and BNTO respectively, but there is a need to explore the control of these defects during growth. Uncontrolled defect propagation causes the type and density of defects to vary considerably between samples, between grains within a sample, and even between neighbouring regions of a single grain. This variability highlights the need for strategies that deliberately regulate and tune structural defect populations in order to control and enhance the associated emergent properties.

In this work, B6TFMO thin films were grown on miscut vicinal sapphire substrates with off-axis cuts ranging from 0.2 ° to 10 °. *M*-plane sapphire was chosen as the substrate for this work for several reasons. It is low-cost, readily available, chemically inert, and has been extensively used for growing these films with considerable success [7]. The m-plane sapphire orientation presents a 0.476 nm hexagonal (equivalent to 0.476 nm × 0.406 nm rectangular) lattice to the growing layer, which approximates a 5.5 Å square [31] for *c*-axis oriented Aurivillius films. This represents a poor lattice match (∼22% mismatch), and therefore film growth is non-epitaxial. However, the film is constrained to *c*-axis orientation by the strongly layered nature of the growing structure. In both non-epitaxial [32] and epitaxial [33] vapour-phase film growth, layer propagation is generally mediated by nucleation at terraces and step-flow growth. Such vicinal cuts have been extensively employed in Si [34] and high-Tc superconductor oxide thin films [35] to control epitaxy and defect formation. Vicinal substrates have also been applied

to perovskite oxides [36] to manipulate strain and interface properties; however, their systematic use to engineer defect topologies in Aurivillius multiferroics remains unexplored. This work addresses this gap by employing vicinal sapphire to controllably modulate OPB defect density and thus polar topology formation in B6TFMO. Engineered step-terrace structures promote step-flow growth during DLI-CVD and provide preferential nucleation sites that enable control over defect formation in the growing film. The resulting films were used to elucidate how defect position, spacing and density govern the emergence of exotic nominally charged domain walls and polarisation patterns consistent with polar vortices in B6TFMO, and how these defect-driven topologies influence the ferroelectric response.

2. Experimental

Detailed descriptions of deposition conditions, precursor preparation, substrate preparation, and all characterisation methodologies are provided in supporting information Section SI1. In this section, we provide an overview of the key experimental parameters and rationale. Aurivillius phase thin films with a nominal stoichiometry of $Bi_6Ti_{2.8}Fe_{1.52}Mn_{0.68}O_{18}$ were synthesised by DLI-CVD on sapphire substrates with miscut angles of 0.2°, 0.5°, and 10°. Films were deposited using a 22% bismuth excess to compensate for volatile bismuth loss, followed by post-annealing at 850 °C to achieve crystalline Aurivillius phase films. Structural characterisation was performed using x-ray diffraction (XRD), scanning transmission electron microscopy (STEM), and atomic force microscopy (AFM). XRD patterns were indexed using reference data for the $m = 5$ Aurivillius phase [8, 37], and DIFFaX simulations were used to examine how c-axis stacking disorder associated with $m = 4$ and $m = 6$ intergrowths modifies the 00 l diffraction profiles [38]. Piezoresponse force microscopy (PFM) was used to investigate ferroelectric domain structure. Further details are provided in the supporting information section SI1.

3. Results and discussion

3.1. Simulations of XRD patterns of layered Aurivillius structures with defect-induced non-periodic regions

When OPB defects are incorporated into the $m = 5$ B6TFMO layered structure, the usual five-layer perovskite stacking sequence is locally disrupted, producing regions in which the number of perovskite layers between adjacent $[Bi_2O_2]^{2+}$ interlayers deviates from five, as illustrated in figure 1. In the simplest case, the lattice on one side of an OPB is shifted by a c-axis displacement, δ, of typically ≈0.4 nm [39] relative to the other side, creating a sharp out-of-phase step between two otherwise well-ordered $m = 5$ blocks. Wider stacking-fault regions can host local $m = 4$ or $m = 6$ intergrowths, where one perovskite layer (∼0.411 nm [40]) is deleted ($m = 4$) or inserted ($m = 6$) between $[Bi_2O_2]^{2+}$ fluorite layers, creating structurally non-periodic segments within the predominant $m = 5$ Aurivillius phase. In more complex OPB/stacking-fault combinations, the OPB terminates such an $m = 4$ or $m = 6$ intergrowth, so that the effective displacement is the sum of the OPB shift (≈0.4 nm [39]) and the additional (or missing) perovskite layer (∼0.411 nm [40]), giving δ ≈0.8 nm; these larger displacements are expected to make a strong contribution to the observed XRD peak profile distortions. When such defects are spatially isolated or randomly distributed, the film maintains an average long-range periodic order, but the presence of local non-periodic regions leads to XRD peak splitting, broadening, or asymmetry rather than a loss of diffraction intensity. This behaviour has been reported for $m = 3$ and $m = 4$ Aurivillius phases, where local deviations from perfect stacking give rise to enhanced scattering and peak broadening, providing a fingerprint of increased stacking disorder, which may contribute to peak broadening alongside finite crystallite-size effects [13, 14, 39, 41].

Motivated by these observations, DIFFaX [38] was employed to simulate $m = 5$ Aurivillius structures containing $m = 4$ and/or $m = 6$ stacking faults, in order to identify which reflections are most sensitive to stacking-fault defects. DIFFaX treats the crystal as a sequence of stacked layers and recursively computes the diffracted intensity, allowing the effect of specific fault types and positions along the c axis to be probed. However, because DIFFaX treats the structure as a one-dimensional stacking sequence, it does not capture the finite lateral extent or strain fields associated with localised OPB cores.

The DIFFaX models were first benchmarked against reference Aurivillius structures, confirming that the simulated 00 l peak positions and relative intensities reproduce those derived from experimental diffraction data (see supporting information section SI 2, figure S1 and table S1) [8, 37]. Building on this validated basis, simulations of faulted $m = 5$ structures (figure S2) show that reflections such as

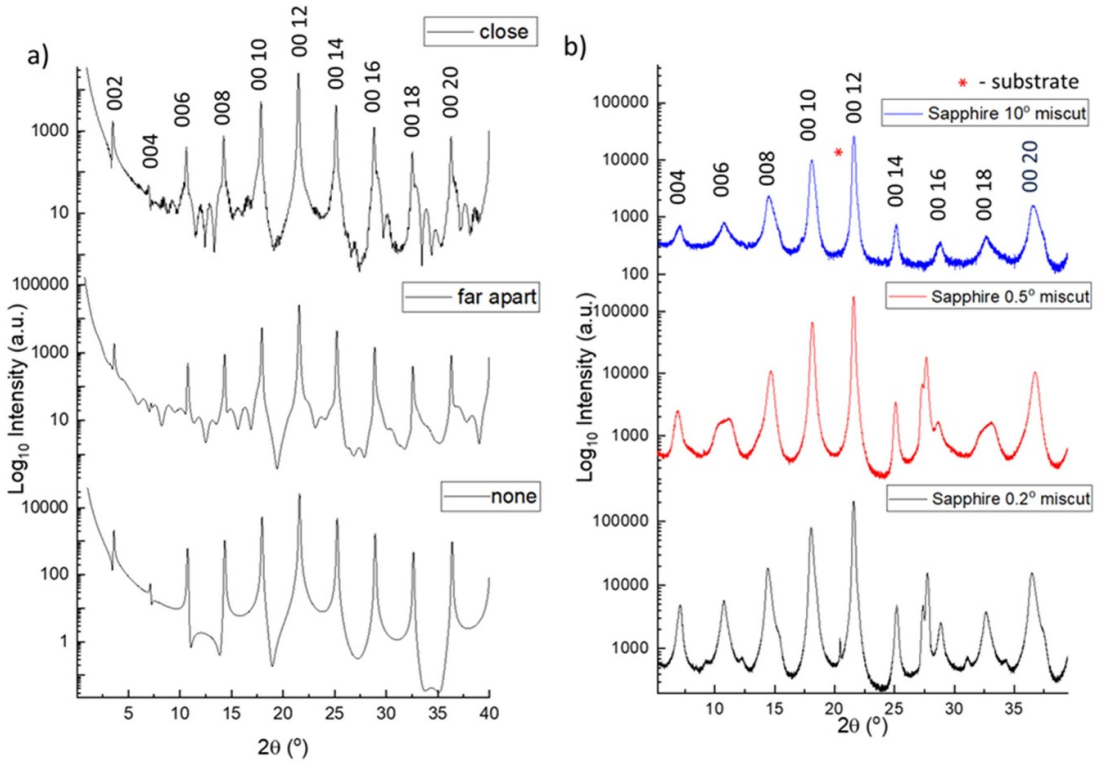

Figure 2. (a) DIFFaX-simulated XRD patterns (Gaussian instrumental broadening of 0.18°) for an $m = 5$ Aurivillius phase. Bottom: defect-free $m = 5$ structure. Middle ('far apart'): two intergrowths (one $m = 4$, one $m = 6$) positioned near opposite film interfaces (19.5 unit cells apart). Top ('close'): $m = 4$ and $m = 6$ intergrowths near the film centre (1.5 unit cells apart). Schematics of these intergrowth positions within the $m = 5$ structure are shown in figure S3. (b) Experimental XRD patterns of B6TFMO films grown on sapphire substrates with vicinal miscut angles of 0.2° (black), 0.5° (red), and 10° (blue).

006, 008, 00 16, 00 18 and 00 20 are particularly sensitive to the inclusion of half-unit-cell $m = 6$ intergrowths, developing pronounced broadening and asymmetric shoulders as the defect density increases. In contrast, reflections such as 00 12 remain comparatively sharp, indicating that not all 00 l peaks respond equally to local stacking disorder.

Further simulations tracking a single $m = 6$ intergrowth at different positions within a 24-unit-cell stack reveal that defects located near the film interfaces induce the strongest perturbations to the calculated XRD patterns, with additional shoulders and oscillations appearing around the defect-sensitive reflections (see supporting information, figure S2). To construct a more realistic defect landscape that better resembles the experimental data, a second stacking fault was introduced into the DIFFaX structure file (see supporting information figure S3) to incorporate a half-unit cell $m = 4$ intergrowth alongside the $m = 6$ defect. Simulations including both half-unit-cell $m = 4$ and $m = 6$ intergrowths demonstrate that the spacing between these intergrowths strongly influences peak broadening: when widely separated (19.5 unit cells apart), only minor shoulders develop on selected reflections, whereas close spacing (1.5 unit cells apart) produces pronounced broadening and asymmetric shoulders consistent with OPB-induced splitting, particularly for the 006, 00 16 and 0018 peaks (figure 2(a)). These features cannot be indexed to any periodic Aurivillius phase and instead arise from scattering by partially disordered finite stacks, where the recursive fault sequence drives complex line-shape evolution. Collectively, the simulations indicate that broadening and asymmetric shoulders consistent with OPB-induced splitting of the 006, 008, 00 16, 00 18, and 00 20 reflections are reliable indicators of a high density of OPB-related intergrowths in $m = 5$ B6TFMO films.

3.2. Experimental investigations of crystallographic properties and morphology of B6TFMO films with defect-induced non-periodic regions

Variations in surface step geometry have been shown to influence the growth behaviour of both perovskite and Aurivillius phases, particularly in epitaxial systems, and can be used to tune their structural and ferroelectric properties [30, 42–44]. The atomic-scale topography of the substrate surface promotes OPB defect nucleation via a steric mechanism during thin-film deposition [13] introducing a phase shift along the layering axis that allows OPB defects to propagate through films up to half a micron thick.

To deliberately encourage OPB defect formation and the associated intergrowths and stacking faults, B6TFMO thin films were grown on vicinal sapphire substrates with off-axis cuts of 0.2°, 0.5°, and 10° (supporting information figures S4 and S5). Although B6TFMO (pseudocubic $a \approx 0.389$ nm), exhibits a large mis-match with sapphire ($a \approx 0.4758$ nm; +22. 3% mismatch), the films are constrained to c-axis orientation by the strongly layered Aurivillius structure. Sapphire provides mechanical stability and chemical robustness at Aurivillius phase crystallisation temperatures. These vicinal cuts promote terrace-mediated step-flow growth [45], a general mechanism in both epitaxial and non-epitaxial vapour-phase growth, and provide controlled atomic step densities that modulate OPB defect nucleation probability and spacing through geometric/kinematic mechanisms at terrace edges. Nuclei on adjacent terraces can become c-axis out of phase, with the phase offset determined by the substrate step height, yielding OPB defects at terrace junctions. Higher miscut angles thus systematically increase step-edge density and defect formation, although very large miscuts (>10°) risk step bunching and surface roughening that complicate growth morphology. During the 850 °C post-growth anneals essential for B6TFMO crystallisation, bismuth migrates and out-diffuses from the film. This bismuth loss triggers crystallographic shear that generates structural defects such as OPBs, which in turn serve as fast diffusion paths for further bismuth volatilisation [13]. The following experiments examine how sapphire miscut angle controls sub-unit-cell defect formation in B6TFMO thin films.

DIFFaX simulations of an $m = 5$ Aurivillius phase containing $m = 4$ and $m = 6$ intergrowth layers (figure 2(a)) were compared with experimental XRD patterns of B6TFMO thin films grown on sapphire substrates with varying miscut angles (figure 2(b)). While DIFFaX effectively models one-dimensional stacking sequences, it does not capture the finite lateral extent or three-dimensional strain fields associated with localised OPB defects; however, it provides useful insight into how c-axis non-periodicity affects the 00 l diffraction profiles.

For all films, the XRD profiles correspond overall to (00 l) textured $m = 5$ Aurivillius phases, with 00 10, 00 12, and 00 14 reflections remaining relatively sharp/symmetric in both simulations (figure 2(a)) and experiments (figure 2(b)), confirming these peaks are largely insensitive to the structural defects. Even films on 0.2° miscut sapphire exhibit broadening and asymmetric shoulders on the 006, 008, 00 18 and 00 20 peaks alongside apparent peak splitting of the 00 16 reflection, consistent with OPB-related defects predicted by simulations (figure 2(a), supporting information figure S2(a)). Films grown on 0.5° miscut sapphire exhibit markedly broader 006 and 00 18 reflections, with full width at half maximum (FWHM) values increasing by approximately 180% and 141%, respectively, relative to films on 0.2° miscut substrates (figure 2(b), supporting information table S2). Rocking curve measurements of the 006 peak (supporting information figure S6) further confirm the progression with the FWHM increasing from 0.22° for B6TFMO on 0.2° miscut sapphire to 0.40° for B6TFMO on 0.5° miscut sapphire. This progressive broadening becomes even more pronounced in B6TFMO films on 10° miscut substrates (supporting information table S2), where peak widths increase and intensities decrease further. The trend reflects the systematically increasing defect density associated with higher substrate step densities. The DIFFaX simulations reproduce the main qualitative features of the experimental peak-profile evolution, supporting the interpretation that deviations from ideal $m = 5$ periodicity increase across the vicinal substrate series. The observed peak broadening and asymmetry thus directly reflect the substrate-controlled OPB evolution, consistent with predictions from the analytical model.

While the DIFFaX simulations successfully reproduce the experimentally observed peak shapes and splittings across the series, quantitative differences in absolute peak intensities arise from variations in atomic site occupancies and cationic displacements in the actual films relative to the idealised [37, 46, 47] structural model employed in the simulations. Such intensity discrepancies [39], which are sensitive to local atomic configurations, do not compromise our interpretation of the defect-driven peak broadening and asymmetry, which encode the meso-scale structural disorder that is the focus of this study.

An analysis of the defects and their densities has been conducted. (supplementary information SI 4, figure S7). Average c-axis lattice parameters of 4.63–4.81 nm (±0.03 nm) were estimated from the images for the 0.2° and 0.5° miscut substrates, respectively. These are slightly smaller than the average value of $c = 4.92 \pm 0.3$ nm estimated from the XRD peaks, probably reflecting systematic errors in magnification on the STEM images. For the same images, we estimate layer defect step heights of 0.43–0.78 nm for the B6TFMO films on 0.2° miscut substrates, and 0.41 nm for films on 0.5° miscut substrates, respectively. Applying Whatmore *et al*'s [39] model ($l\, n\frac{c}{2}$ where n is an odd integer) to these B6TFMO films and using $c = 4.9$ nm) provides a compelling explanation for the selective peak splitting observed in figure 2(b). A key advantage of this model is its power: given a measured δ value, to predict which 00 l reflections will exhibit splitting or broadening. For the smallest displacements of $\delta \approx 0.4$ nm, characteristic of pure OPBs, the period predicts splitting at the 006 and 00 18 reflections. An intermediate $\delta \approx 0.78$ nm perturbs the 00 16 peak. Finally, the largest displacements of ≈0.87 nm from

Table 1. Structural evolution across the vicinal substrate series, showing the transition from Laue oscillations at 0.2° miscut to defect-induced asymmetric broadening at 0.5° and 10° miscut. HAADF-STEM-derived step spacing provides a semi-quantitative estimate of local defect density, while XRD captures the film-averaged peak evolution.

Substrate Miscut	Peak character	XRD signature	STEM-derived defect spacing/density	Defect density and interpretation
0.2°	Sharp peaks with periodic Laue oscillations	Coherency fringes on 006, 00 18; peak broadening at 008, 00 20; peak splitting at 00 16	Mean step spacing: 20.80 ± 0.30 nm; local defect density: 0.02 defects nm^{-2}	Low-moderate defect density; localised simple OPBs ($\delta \approx$0.4 nm) and composite OPB/stacking-fault complexes ($\delta \approx$0.78 nm) coexist; long-range *c*-axis periodicity preserved
0.5°	Broad peaks with asymmetric shoulders; complete loss of Laue oscillations	Peak broadening at 006, 008, 00 18, 00 20; peak splitting at 00 16	Mean step spacing: 9.72 ± 0.06 nm; local defect density: 0.05 defects nm^{-2}	High defect density; step defect types ($\delta = 0.41$ nm) active; defect-induced disruption of *c*-axis periodicity dominates
10°	Persistent asymmetric broadening; complete loss of Laue oscillations	Severe broadening across reflections (exception 00 12)	Not reliably quantified by STEM	High defect density persists; defect-induced disorder remains dominant broadening mechanism

OPB/stacking-fault complexes produce a period that drives splitting/broadening at the 008 and 00 20 reflections. This defect-specific sensitivity elegantly fingerprints the coexisting populations of simple OPBs versus composite defects across the vicinal substrate series, directly validating the model's utility for defect analysis in Aurivillius thin films.

The satellite features visible in figure 2(b) directly reveal the transition from crystalline coherence to defect-induced disorder as substrate miscut increases. The 0.2° miscut film exhibits periodic Laue oscillations (coherency fringes) superimposed on the 006 and 00 18 reflections, indicating good crystalline coherence despite the presence of localised defects. These fringes arise from the finite film thickness (94 nm) and reflect long-range *c*-axis periodicity preserved at low defect density. In contrast, the 0.5° and 10° miscut films completely lose this periodic oscillation structure, displaying instead asymmetric broadening and shoulders, characteristic of defect-induced disruption of *c*-axis periodicity. This loss of Laue coherence directly correlates with increasing defect density: the 0.5° miscut shows maximum peak complexity where all defect types ($\delta = 0.41$ nm, 0.82 nm, and 0.88 nm) are simultaneously active, while the 10° miscut maintains severe peak broadening, confirming that defect-induced disorder remains the dominant mechanism. The systematic evolution from periodic Laue fringes (0.2° miscut) to severe asymmetric broadening (0.5° to 10° miscut) thus directly encodes substrate-controlled engineering of defect landscapes across the vicinal substrate series (table 1). Average film thicknesses across the substrates were 94 ± 26 nm, 112 ± 22 nm, and 94 ± 11 nm for B6TFMO films on 0.2°, 0.5°, and 10° miscut sapphire, respectively. These thicknesses are essentially equivalent within the experimental error of measurement, ruling out thickness variations as the primary cause of peak broadening.

AFM analysis [48] of film surfaces (supporting information figure S8) reveals systematic grain areas reduction (0.49 $\mu m^2 \rightarrow$ 0.30 $\mu m^2 \rightarrow$ 0.26 μm^2) with increasing substrate miscut angle. However, the modest grain area reduction from 0.5° to 10° miscut (0.30 $\rightarrow$ 0.26 μm^{-2}) is insufficient to account for the severe and persistent XRD peak broadening observed at 10° miscut. This observation directly demonstrates that defect-induced disorder, not grain area reduction, is the dominant broadening mechanism across the series. Both metrics independently reflect consequences of increased substrate step density: AFM captures in-plane morphological effects (grain nucleation and refinement via step-mediated growth), while XRD reveals out-of-plane effects (OPB defect proliferation causing asymmetric peak broadening in the 00 l reflections). Our DIFFaX simulations employ a 1D stacking model that directly predicts this peak broadening from defect density, bypassing grain area effects entirely. This 1D approach is justified because (i) XRD interrogates average structures along the c^* reciprocal axis, (ii) the model successfully reproduces observed 00 l reflection evolution by varying only defect types and frequencies, not grain areas, and (iii) the quantitative agreement between simulation and experiment validates the defect-driven interpretation. Out-of-plane effects perpendicular to the *c*-axis (e.g. in-plane lattice distortions and lateral defect distributions in the *a*-*b* plane) are separately interrogated by STEM

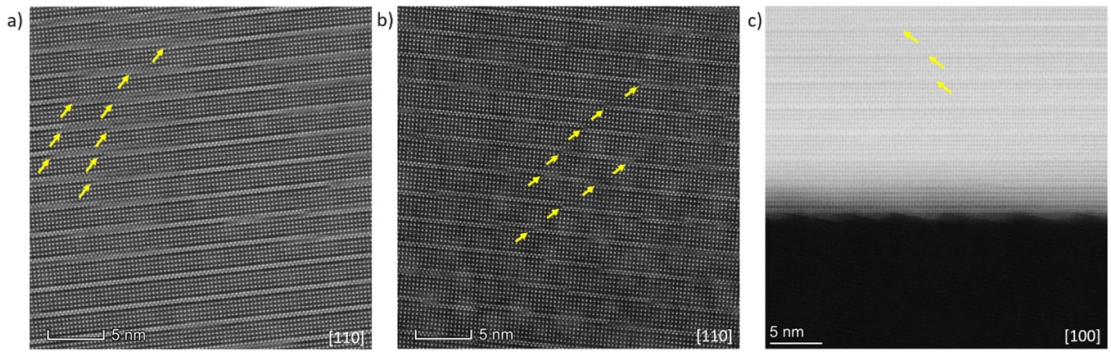

Figure 3. STEM images of the B6TFMO films on (a) 0.2 °, (b) 0.5 ° and (c) 10 ° mis-cut sapphire. OPB defects are observed in all films. The yellow arrows point to some examples of these defects within the images.

(section 3.3). The systematic XRD peak evolution therefore translates substrate-controlled defect engineering, with grain area refinement serving as a secondary morphological consequence rather than the primary cause of XRD broadenings.

AFM (supporting information figure S8) and STEM imaging reveal that the non-epitaxial B6TFMO films exhibit relatively rough surfaces, with average RMS roughness values of 32.00 ± 2.71 nm (0.2° miscut), 19.64 ± 0.91 nm (0.5° miscut) and 21.83 ± 1.27 nm (10 ° miscut) sapphire substrates, determined from five 10 μm x 10 μm scans per sample. Cross-sectional STEM (supporting information figure S5) confirms that films remain continuous across all miscut angles, with this roughness arising from two primary contributions: surface microcrystallites (two-dimensional islands several Aurivillius unit cells tall) [49, 50] and variations in underlying grain orientation resulting from the overlapping lamellar grain architecture characteristic of Aurivillius growth.

For B6TFMO films on the 10° miscut substrate, surface roughness is dominated by grain orientation effects (supporting information figures S5 and S8). Two distinct grain families emerge: grains that grow approximately parallel to the substrate surface (0° tilt) and grains tilted ∼10° along the vicinal step direction, with an apparent in-plane rotation between the two families (figure S9). The tilted grains exhibit pronounced thickness variations along their length (e.g. 48 nm to 104 nm within a single grain; figure S5(b)), directly contributing to surface height modulation.

3.3. Atomic scale visualisation of sub-unit-cell defects in B6TFMO films

Atomic-resolution cross-sectional STEM imaging of B6TFMO films on vicinal sapphire substrates reveals sub-unit-cell defects, including OPBs and stacking faults, in all samples (figure 3). STEM provides local structural information that complements the film-averaged defect trends obtained from XRD. Cross-sectional HAADF-STEM images were used to estimate local defect spacing in the 0.2° and 0.5° miscut films (figures 3(a), (b)), supporting information Section SI 4, figure S7, table 1). The mean step-related spacings were approximately 20.8 nm and 9.7 nm, respectively. The images provide direct visual evidence consistent with the displacement magnitudes, δ, predicted by XRD peak profile (Whatmore *et al* [39]). For the 0.2° film, the observed step heights of 0.78 nm and 0.4 nm indicate that the (00 l) reflections expected to be doubled include 006 and 00 18 for the smaller displacement, and 00 16 for the larger displacement. For the 0.5° film, the measured step height of 0.4 nm predicts doubling of 006 and 00 18. These local measurements (figure S7) are consistent with the increasing XRD broadening and peak splitting observed with increasing vicinality (supporting information table S2). The estimated defect density for the 0.5° miscut film (0.05 defects nm^{-2}) is approximately twice that of the 0.2° film (0.02 defects nm^{-2}), consistent with the stronger XRD broadening observed in figure 2 and table S2. Because STEM probes only local regions, these densities should be regarded as semi-quantitative. The broader miscut-dependent disorder trend is more robustly established by the film-averaged XRD line-shape analysis.

The inverse relationship between defect spacing and XRD peak breadth provides a semi-quantitative link between the STEM- and XRD-derived structural metrics. The mean defect spacing decreases from 20.8 nm in the 0.2° film to 9.7 nm in the 0.5° film, corresponding to a ratio of 2.1:1. This is broadly consistent with the experimentally measured FWHM ratios for the most step-sensitive reflections, namely 2.8:1 for 006 and 2.4:1 for 00 18 (supporting information table S2). By contrast, the much smaller ratio for 008 (1.2:1) indicates weaker sensitivity to the planar step defects present (it would only be observed for $\delta \approx 0.87$ nm) and a larger contribution from other disorder sources. Suitable HAADF-STEM images were not available for reliable quantitative analysis of the 10° miscut film (figure 3(c));

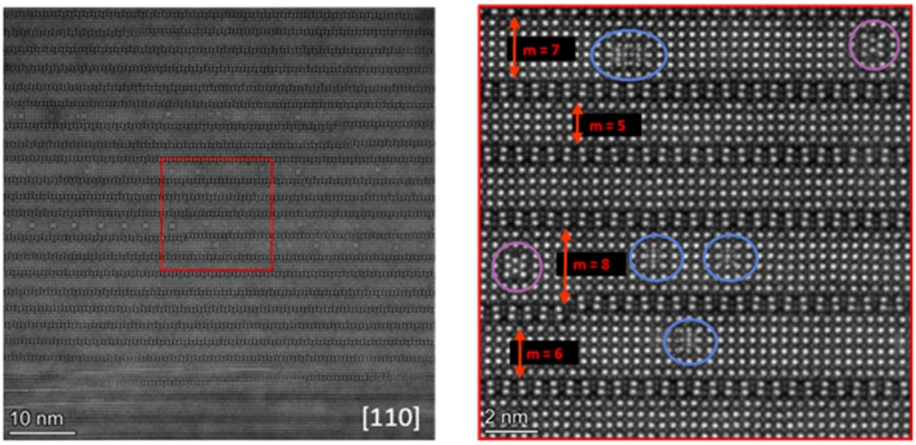

Figure 4. HAADF STEM images showing planar 'anatase'-type regions in a B6TFMO film on 0.2 ° mis-cut sapphire substrate near the top of the B6TFMO film. Within this region, the number of m perovskite-like unit cells between the dielectric interlayers varies from 4 to 8. When there are 7 or more perovskite unit cells, a nanorod-type precipitate (blue and purple circles) is also observed.

however, its more pronounced disorder is consistent with the XRD trends. For the 10° film, the broadening ratios relative to the 0.2° sample are similar for the 006, 008 and 00 18 reflections (1.9:1, 1.7:1 and 1.8:1, respectively), suggesting a more distributed disorder landscape rather than one dominated by the same step-defect mechanism that governs the lower-miscut films. Beyond the OPBs and stacking faults observed across all samples (figure 3), high-magnification imaging (figure 4 and supporting information figure S10) identifies low-angle grain boundaries (<15°) decorated with bismuth-deficient 'anatase'-like planar defects, where $[Bi_2O_2]^{2+}$ interlayers are replaced by edge-sharing BO_6 octahedra featuring double Bi^{3+} columns [22, 51, 52]. These defects exhibit variable perovskite block counts (m = 4–8) and the 'anatase'- type interfaces measure 0.84–0.90 nm, in good agreement with the δ = 0.87 nm displacement associated with the 008/00 20 peak splitting discussed above (Whatmore *et al* [39]).

Regions with ⩾6 perovskite blocks host bismuth-deficient 'nanorod' [53] precipitates penetrating the perovskite layers (figure 4), matching defects reported in higher-m Aurivillius phases and $BiFeO_3$ [53–58]. Composed of paired central Bi atoms, these nanorod defects (MacLaren *et al* [53]) are accompanied by BO_6 to BO_5 square pyramid transitions at their edges, likely driven by internal strain imparted by the nanorod core. Nanorod precipitates in figure 4 confirm MacLaren *et al*'s [53] assessment that these defects do not necessarily span the full film thickness. Distinct precipitates with paired central Bi atoms are visible at the inset edges (purple circles), while central regions (blue circles) show mixed precipitate-Aurivillius character, indicating the defects are finite-length lamella-spanning features. The cores likely comprise strained Bi_2O_3-like structures flanked by Ti-rich columns.

These Bi-deficient nanorods appear selectively in $m \geqslant 6$ intergrowths and grain boundaries. Two complementary mechanisms for nanorod formation are proposed [1]: Bi^{3+} out-diffusion along low-angle grain boundaries during the 850 °C anneal, creating Bi-poor 'anatase'-like interfaces; and [2] local structural reorganisation to stabilise extended m = 6–8 intergrowths, where nanorod precipitates may supply the additional Bi^{3+} needed for higher-m phase stability. These observations highlight the interplay between volatility-driven chemistry and defect accommodation in Aurivillius thin films.

3.4. Atomic resolution mapping of polar topologies of layered Aurivillius phase thin films with defect-driven non-periodic regions

As shown previously for Aurivillius phases, disruptions of the periodic lattice by OPBs and stacking faults generate pronounced internal elastic and electrostatic gradients, enabling extraordinary polarisation states such as nominally charged domain walls [30], non-trivial polarisation rotations, and polar vortex-like textures [24]. Building on this, the present work extends atomic-scale polarisation mapping to B6TFMO films grown on vicinal sapphire, where OPB density and spacing are deliberately tuned via substrate miscut.

In these vicinally grown B6TFMO films, the local polarisation within individual perovskite cells is quantified by mapping B-site cation displacements from centrosymmetric positions. Atomic-resolution vector mapping is used to determine how OPB position, separation, and density control the formation of exotic 180° nominally charged domain walls and vortex-like polar textures. Polarisation mapping of HAADF-STEM images (figure 5, supporting information figure S11) shows that OPBs in films on

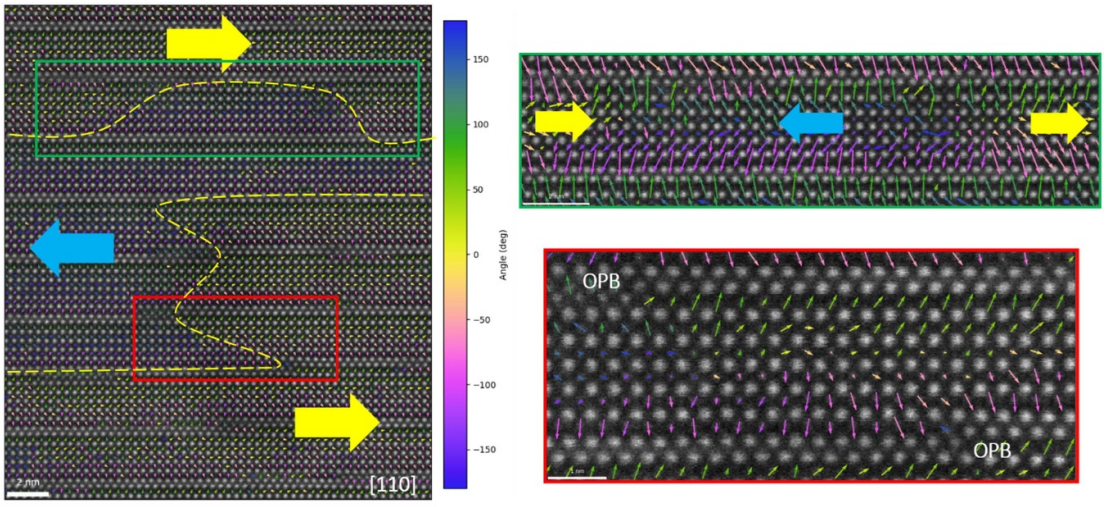

Figure 5. HAADF-STEM images of B6TFMO thin film on 0.2 ° miscut sapphire where polarisation displacement vectors of the B-site cation are mapped using TEMUL toolkit [55]. In this figure, the colour of the arrow indicates the direction that polarisation is pointing in, with yellow arrows (orientated 0 °) indicating that polarisation is pointing towards the right and with blue arrows (orientated 180 °) indicating that polarisation is pointing towards the left. In the insets, the size of the arrow correlates to the magnitude of the displacement of the B-site cation. The dashed yellow curved line gives an approximate location of nominally charged domain walls within the image. The large arrows indicate an approximate overall direction of polarisation within the ferroelectric domains present. Green inset: shows an enlarged region of nominally charged 180 ° head-to-head and tail-to-tail domain walls. Red inset: shows polarisation patterns consistent with a polar vortex-like configuration in a region containing a nominal 180 ° tail-to-tail charged domain wall between two OPB defects.

mis-cut sapphire routinely nucleate nominally 180° charged head-to-head (H–H) and tail-to-tail (T–T) domain walls extending over multiple perovskite layers. The dashed yellow line in figure 5 marks one such domain wall, whose trajectory is clearly anchored to an OPB traversing the film thickness, confirming that OPBs in vicinally grown B6TFMO act as structural pathways along which nominally charged domain walls can be stabilised.

The present work provides further evidence for the formation of polarisation patterns consistent with polar vortex-like structures in newly synthesised B6TFMO films on vicinal miscut substrates, where vicinal growth promotes OPB-rich microstructures. As shown in figure 5, polarisation configurations reminiscent of polar vortices are stabilised between two OPB defects separated by approximately five to twelve perovskite unit cells (∼3–5 nm) and with heights of 2.4–2.8 nm (half-unit-cell thick m = 5 and m = 6 blocks). The vortex-like structure size is comparable to that reported previously in B6TFMO, demonstrating that such configurations are robust, and that engineered OPB defect arrays on vicinal substrates provide an additional degree of freedom for reproducibly positioning and sizing polar vortex-like polarisation patterns. Similar vortex-like configurations are also identified in films grown on 0.5° miscut substrates (see supporting information figure S11), underlining that polarisation patterns reminiscent of polar vortices is a general feature of OPB-rich B6TFMO, not an isolated case. In a true vortex state, the polarisation rotates continuously about a vortex core, producing an inhomogeneous polarisation distribution that differs from conventional Ising (fixed polarisation axis), Néel, or Bloch-type (fixed polarisation magnitude) domain walls. The textures observed here resemble vortex domain walls rather than simple flux-closure states, with both the magnitude and direction of the polarisation varying smoothly around the core.

Recent work by Dutta *et al* [59] on $Bi_4Ti_3O_{12}$ established the atomic-scale mechanism for OPB-mediated enhancement of vertical polarisation, with DFT showing that OPBs disrupt the stacking of $(Bi_2O_2)^{2+}$ layers and perovskite-like slabs, inducing B-site off-centring, Bi displacement along *c*, modified Ti–O bond lengths and octahedral tilts, and local symmetry lowering that enhances the *c*-axis polarisation. Corresponding electron localisation maps reveal local charge redistribution and strengthened Bi–O covalency, consistent with defect-stabilised polar discontinuities that favour nominally charged domain wall nucleation. The present B6TFMO study complements this by demonstrating that OPBs introduced in films grown on vicinal substrates not only enhance vertical polarisation but also provide preferred pathways along which charged domain walls and vortex-like states are stabilised.

In ferroelectrics, charged domain walls carry large bound charge and normally require compensation by mobile charges, defects or electronic reconstruction [27, 28]. Calculations for B6TFMO [24] indicate that perfectly planar H–H and T–T 180° walls are energetically costly, and that bending of the wall

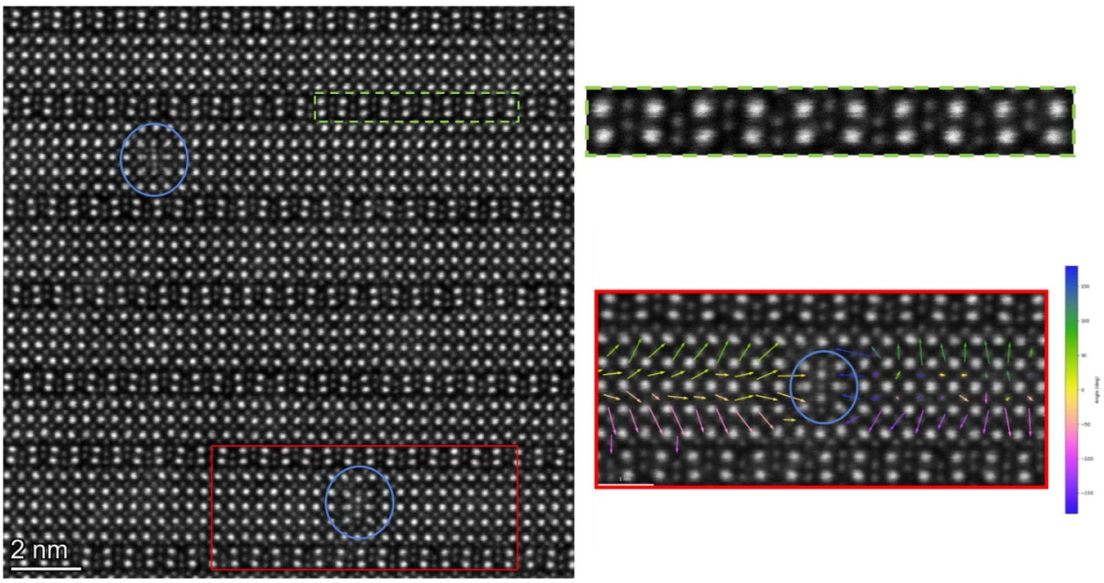

Figure 6. HAADF STEM imaging of an area with 'anatase'- type planar defects replacing the $[Bi_2O_2]^{2+}$ interlayer within a B6TFMO thin film on 0.2 ° sapphire. The 'anatase'- type defect can be seen in more closely in the green dashed inset. In the red inset the polarisation displacement vectors of the B-site cation are mapped using TEMUL toolkit [60]. In the red inset, the colour of the arrow indicates the direction it is pointing in, with yellow (0°) pointing towards right and blue (180°) pointing towards the left, while the size of the arrow correlates to the magnitude of the displacement of the B-site cation. Within this image 'anatase'-like interlayers composed of BO_6 octahedra forming 's'-shaped tunnels are interleaved between perovskite unit cells. Nanorod precipitates, circled in blue are also present within the perovskite blocks where the B-site cations adjacent to the precipitates are highly strained with the polarisation vectors pointing towards the defect, generating polarisation patterns reminiscent of anti-hedgehog-like configurations.

while remaining charged is required to reduce the energy. This is fully consistent with the inclined 180° domain walls observed here, which bow between OPBs rather than remaining strictly planar. In addition, prior work on B6TFMO has shown enhanced cation partitioning near OPB defects [24, 25], suggesting local bandgap modulation between domain-wall and bulk regions and raising the prospect of intrinsically conducting charged walls. High-resolution spectroscopy will be required to confirm this scenario.

Beyond this, the present work introduces different classes of defects in B6TFMO: 'anatase'-like planar interlayers and associated nanorod precipitates, and directly links them to polar textures at the atomic scale. Polarisation vector mapping around bismuth-deficient nanorod precipitates (figure 6) shows that polarisation vectors bend away from the nanorod core, with vectors on opposite sides pointing towards the precipitate. This topology is reminiscent of anti-hedgehog states reported by Li *et al* [58] in $BiFeO_3$, which are analogous to polar and magnetic skyrmions. While these local structural features are suggestive of topological order, definitive characterisation of topological states would require complementary techniques such as full three-dimensional reconstruction or theoretical calculations beyond the scope of the present work. The observation of polarisation configurations consistent with skyrmion-like textures pinned to chemically distinct defect cores in B6TFMO on vicinal substrates highlights the broader potential of defect and substrate engineering to stabilise polarisation patterns reminiscent of multiferroic skyrmion-like states, opening new pathways for the design of next-generation multiferroic nanoelectronic devices [24, 58].

3.5. PFM of B6TFMO films with tailored defect levels

To assess how defect-engineered polar topologies in B6TFMO grown on vicinal substrates influence functional ferroelectric behaviour, DART (dual AC-resonance tracking)-PFM [61] was used to probe 90–100 nm thick films (supporting information figure S12). PFM measures mechanical piezoresponse (strain induced by applied electric field) rather than electrical conductivity, providing a direct probe of ferroelectric polarisation. The DART-PFM measurements were performed at high measurement frequencies (∼258 kHz (vertical) and ∼792 kHz (lateral)) and low drive amplitudes (1–3 V_{AC}). This combination of resonance tracking at high frequency, combined with sub-coercive-field amplitudes, optimises detection of genuine piezoelectric response while minimising electrostatic artefacts. To distinguish genuine ferroelectric signals from electrostatic artefacts, we employed multi-modal (lateral and vertical) domain correlation and phase contrast analysis, as detailed below.

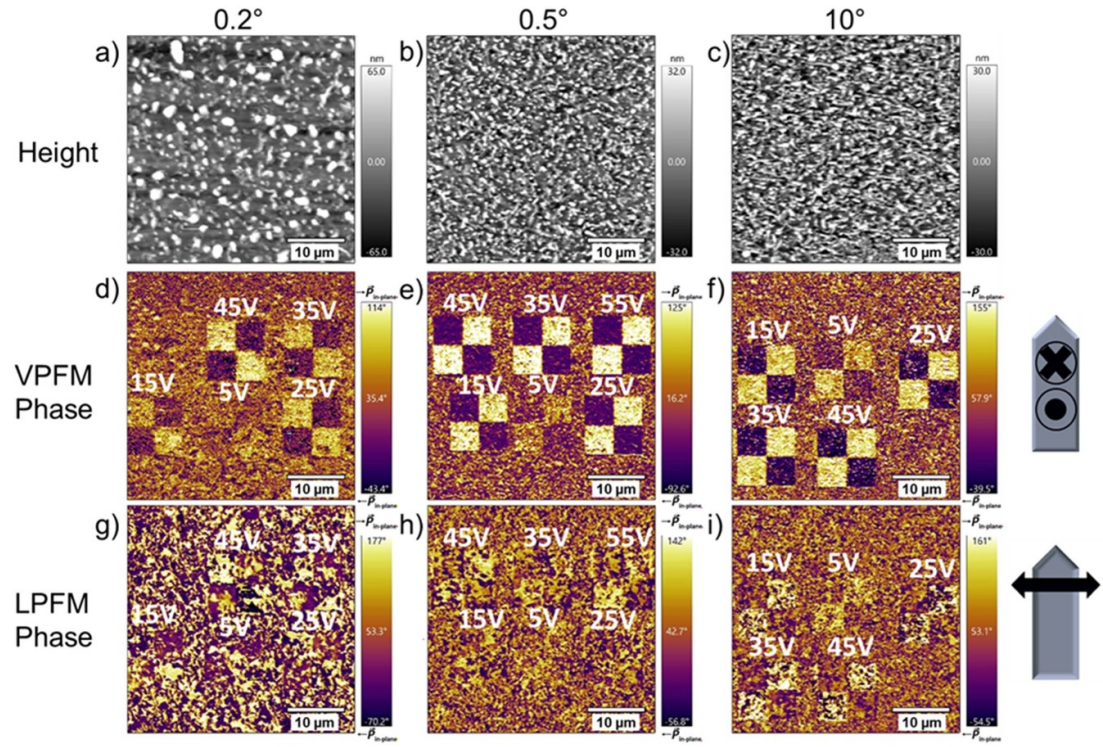

Figure 7. Ferroelectric poling of B6TFMO on 0.2 °, 0.5 °and 10 ° mis-cut sapphire substrates using applied biases of ± 5 V_{DC} to ± 55 V_{DC} over 10×10 μm^2 regions.

In even-layered Aurivillius phases, the spontaneous polarisation is constrained to the in-plane *b*-axis by a horizontal mirror plane, whereas in odd-layered $m = 5$ B6TFMO this mirror symmetry is broken, permitting a weak out-of-plane *c*-axis component superimposed on the dominant in-plane *b*-axis polarisation [62], as observed in the lateral piezoresponse force microscopy (LPFM) and vertical piezoresponse force microscopy (VPFM) images in supporting information figure S12. In these films, electrostatic interactions that would favour straight, flat domain walls are insufficient to overcome the domain wall energy landscape, which instead favours curved and meandering domain configurations observed in the PFM data, consistent with prior observations in Aurivillius systems [63].

PFM imaging (supporting information figure S12) shows all three films are naturally self-polarised, with progressively smaller ferroelectric domains at higher miscut angles: 0.233 ± 0.025 μm^2, 0.210 ± 0.004 μm^2 and 0.139 ± 0.012 μm^2 for the B6TFMO films on 0.2°, 0.5° and 10° miscut sapphire substrates respectively. This systematic grain area-domain area correlation mirrors the AFM trend (0.49–0.26 μm^2 grain area): smaller grains impose smaller ferroelectric domains due to increased grain boundary pinning.

Higher-miscut films exhibit elevated structural disorder from dense OPBs/intergrowth defects and abundant grain boundaries, which serve as Bi fast-diffusion paths during the 850 °C anneal (supporting information figure S10) [13]. While single OPBs may not create domain walls, defect ensembles generate local polar discontinuities [24] that act as domain nucleation sites [63]. The resulting high defect density thus promotes increased domain wall density, yielding the finest domain structure at 10° miscut (supporting information figure S12).

Figure 7 demonstrates that both vertical and lateral ferroelectric domains in all B6TFMO films are switchable under an applied DC bias. Under the experimental geometry used here, the vertical domains switch more readily. Direct bias application through the vertical PFM tip efficiently reverses the out-of-plane polarisation along the *c*-axis, whereas the trailing field generated during tip scanning produces a weaker, spatially distributed in-plane electric field capable of switching lateral domains [60, 64]. This preferential vertical domain switching arises because, although the Aurivillius structure features a dominant in-plane polarisation component [62], the symmetry-allowed *c*-axis polarisation component is readily accessible to the vertical electric field applied by the PFM tip. Reversal of this *c*-axis component perturbs the local lattice distortion and polarisation rotation pathways, thereby influencing the stability

Table 2. Quantitative ferroelectric switching and structural parameters of B6TFMO film across the vicinal substrate series. Out-of-plane switching voltages decrease three-fold while film thickness remains constant, demonstrating defect-mediated enhancement.

Parameter	0.2° miscut	0.5° miscut	10° miscut	Trend
Out-of-plane switching voltage (V_{DC})	±15	Between ±5 and ±15	±5	3-fold reduction
Out-of-plane switching field (V/nm)	±0.16	Between ±0.05 and ±0.13	±0.05	3-fold reduction
In-plane switching voltage (V_{DC})	±45	±45	±45	Incomplete at all levels; field-geometry limited
Film thickness (nm)	94 ± 26	112 ± 22	94 ± 11	Equivalent (within error)
Average grain area (μm^2)	0.49	0.30	0.26	Decreasing with miscut
Ferroelectric domain area (μm^2)	0.233 ± 0.025	0.210 ± 0.004	0.139 ± 0.012	Decreasing with miscut
Defect-related XRD peak broadening (see table S2)	Lower broadening	Higher broadening	Extensive broadening	Broadening increases with miscut; consistent with rising defect density

and redistribution of in-plane domains. The defect-rich microstructure and geometric field effects in these films further enhance vertical domain switching efficiency relative to in-plane switching.

PFM poling experiments on B6TFMO films grown on 0.2°, 0.5° and 10° miscut sapphire (figure 7, supporting information figure S13) confirm that the out-of-plane response is switchable in all cases after ±15 V_{DC}. Notably, the film on the 10° miscut substrate exhibits out-of-plane switching at significantly lower voltages (±5 V_{DC}), indicating an enhanced switching susceptibility compared with films on lower miscut substrates. To quantify this enhancement, we extract switching field strengths and domain parameters from our PFM measurements, which reveal systematic correlation with structural disorder metrics (table 2). Out-of-plane switching fields decrease from ±0.16 V nm^{-1} (0.2° miscut) to ±0.05 V nm^{-1} (10° miscut)—a three-fold reduction—while film thickness remains constant (94 nm), and this systematic voltage dependence on substrate miscut (15 V for 0.2° to 5 V for 10° miscut) correlates directly with independently measured XRD-defined defect density trends, establishing that defect-controlled microstructure, not film thickness variations, drives the enhanced ferroelectric response. Ferroelectric domain area systematically decreases with increasing miscut angle (0.233 ± 0.025 μm^2 to 0.139 ± 0.012 μm^2), and smaller domains are inherently more responsive to external fields, a classical ferroelectric switching principle demonstrated here across our substrate series.

In contrast, the in-plane component is more difficult to switch. Closer inspection of the in-plane poled region in B6TFMO on 0.2° miscut sapphire (supporting information figure S13) reveals complete out-of-plane domain reversal but only partial lateral polarisation redistribution. Pre-poling, the average in-plane domain size was 0.46 μm (51.6% left, 48.2% right polarised); post −45 V_{DC} poling, domain size increased to 0.99 μm with 53.3% right-polarised domains (46.3% left), indicating net lateral reorientation accompanied by domain growth but no complete switching. Despite applying nine-fold higher voltages than required for out-of-plane switching (±45 V vs ±5 V for the 10° miscut film). This out-of-plane vs in-plane switching disparity reflects both field geometry and defect-domain interactions. VPFM applies a uniform vertical field across the entire film thickness while LPFM generates a localised fringe field concentrated near the scanning tip contact point, resulting in non-uniform lateral field distribution through the film depth.

Moreover, the dominant *b*-axis in-plane polarisation interacts more strongly with structural defects (OPBs, stacking faults, intergrowths, grain boundaries), which serve as effective pinning centres for lateral domain walls. While these defects facilitate out-of-plane switching through local strain and electrostatic gradients that directly align with the c-axis response, they stabilise the in-plane domain configuration against complete reorientation.

The markedly increased out-of-plane switching susceptibility observed in the 10° miscut B6TFMO film, requiring only ±5 V_{DC} compared to higher voltages needed for films on lower miscut substrates (figure 7), can be explained by several microstructural factors.

STEM imaging reveals two distinct grain families in B6TFMO on 10° vicinal sapphire substrates: grains lying grains lying approximately parallel to the substrate (∼0° tilt) and grains tilted by ∼10° (supporting information figure S9), with an apparent in-plane rotation between the two families. In

the ∼10° tilted grains, the dominant in-plane b-axis polarisation vector, which carries the primary spontaneous polarisation in odd-layered m = 5 Aurivillius phases, is rotated ∼10° out of plane. This orientation provides a substantial vertical component that is directly accessible to the vertical PFM tip, substantially enhancing the measured out-of-plane piezoresponse relative to flatter grains in lower-miscut films.

Complementing this geometric advantage, the higher step density promotes abundant OPB defects and stacking faults that create local strain/electrostatic energy gradients, reducing the out-of-plane polarisation switching barrier [24, 59]. These *c*-axis-aligned defects form interconnected networks that facilitate domain wall motion at reduced fields. Smaller grains (0.26 μm^2 at 10° miscut vs 0.49 μm^2 at 0.2° miscut) and dense grain boundaries introduce additional local strain fields and charged domain pinning sites that further decrease coercive fields, while the finer ferroelectric domains (∼0.14 μm^2) prove inherently more responsive to external stimuli.

To validate that this switching represents genuine ferroelectric behaviour rather than leakage-mediated artefacts, we employ three independent strategies [1]: Multi-modal domain correlation: LPFM and VPFM measurements reveal consistent spatial domain patterns, confirming genuine ferroelectric polarisation rather than electrostatic artefacts [2]. Phase contrast validation: PFM phase images exhibit characteristic 180° phase reversal between oppositely polarised domains (figure 7, supporting information figure S13), the hallmark of ferroelectric polarisation [3]. Reversible DC switching with defect-density correlation: the switching voltage dependence on substrate miscut precisely correlates with independently measured XRD-defined defect density/disorder trends, demonstrating that ferroelectric behaviour tracks controlled structural parameters.

If enhanced leakage pathways (due to OPB defects) were dominant, we would expect progressive loss of ferroelectric contrast at high miscuts where defect density is highest. Instead, ferroelectric domain visibility and switching capability are enhanced at higher miscuts. This counter-intuitive trend: improved ferroelectric response with increased defect density, directly contradicts a leakage-artefact interpretation and confirms that OPB defects genuinely enhance ferroelectric properties. STEM observations show that nominally charged domain walls and polarisation patterns consistent with polar vortices form preferentially at OPB defect sites, structurally explaining why increased defect density enhances rather than suppresses ferroelectric functionality. To further rule out confounding variables, films on 0.2° and 10° miscut substrates have identical average thickness (94 nm) yet exhibit dramatically different ferroelectric switching voltages (15 V vs 5 V), demonstrating that substrate-controlled defect density, rather than film thickness variation, drives the observed ferroelectric property evolution. The systematic trends in ferroelectric switching behaviour observed across the vicinal substrate series (figure 7; table 2) demonstrate reproducible substrate-controlled modulation of polar topologies within the current sample set. However, a comprehensive statistical assessment of sample-to-sample variability at each miscut angle would require a larger population of independently prepared films, which represents an important direction for future studies aimed at optimising reproducibility and establishing quantitative variability thresholds for technological applications. The present results establish the fundamental principle that substrate vicinality enables controlled defect-driven engineering of ferroelectric topologies; rigorous reproducibility validation across larger sample populations will be essential for practical device implementation.

4. Conclusions

This study demonstrates that vicinal sapphire substrates provide an effective approach for engineering defect distributions in multiferroic B6TFMO thin films, influencing both structural and polar properties. As the substrate miscut angle increases from 0.2° to 10°, a clear progression emerges: grains grow larger at low substrate miscut angles, while higher substrate miscut angles produce pronounced XRD peak broadening, grain refinement (0.49 μm^2 down to 0.26 μm^2), and finer ferroelectric domains (0.23 μm^2 down to 0.14 μm^2). These changes systematically track the increasing step density that promotes nucleation of OPBs and stacking faults.

Direct STEM measurements of OPB defect displacements (0.4–0.9 nm) quantitatively validate XRD-derived defect displacement values (0.41–0.88 nm). Atomic-resolution STEM imaging further reveals a new type of defect in B6TFMO: nanorod precipitates within ‘anatase’-like interlayers. These structures generate polar textures consistent with anti-hedgehog states reminiscent of skyrmions. Significantly, 180° nominally charged domain walls and polarisation patterns consistent with polar vortices form in close spatial association with OPB defects, with vortex-like structures observed between OPB defects spaced 3 nm to 5 nm apart across multiple films.

This indicates that defect positioning plays a key role in organising these complex polar configurations.

The most striking functional consequence appears in piezoresponse force microscopy, where 10° miscut films exhibit dramatically reduced out-of-plane switching voltages (±5 V). This enhancement arises from the combination of tilted (∼10°) grains, which rotate the dominant *b*-axis polarisation into vertical accessibility for PFM, with a defect-rich microstructure that facilitates out-of-plane domain wall motion while pinning in-plane configurations. The same defects that stabilise lateral domains against switching thus selectively promote vertical response. Future investigations should address the temporal stability, thermal robustness, and electrical cycling endurance of these defect-stabilised topological structures, which will be essential for evaluating their potential in practical device applications.

Taken together, this work reveals substrate vicinality as a master parameter that couples geometric step arrays, defect cascades, topological polar states, and anisotropic switching, providing a reproducible blueprint for designing Aurivillius multiferroics with tailored domain topologies and low-voltage functionality for next-generation nanoelectronics.

Acknowledgment

The authors gratefully acknowledge the support of the Royal Society-Research Ireland University Research Fellowship URF\R\201008, Enhancement Award RGF\EA\180206, and Research Ireland Advanced Laureate Award IRCLA/2023/1842. The authors gratefully acknowledge the support of Tyndall National Institute (TNI) and Ohio State University (OSU) for partly funding this collaboration via the TNI-OSU Catalyst—PILOT PROGRAM award. M.S.C. acknowledges funding from the ERC CoG DISCO grant 101171966, the Royal Society Tata University Research Fellowship (URF\R1\201318), and the Royal Society Enhancement Award RF\ERE\210200EM1.

Data availability statement

All data that support the findings of this study are included within the article (and any supplementary files).

Supplementary data 1 available at https://doi.org/10.1088/2515-7639/ae8642/data1.

Author contributions

Louise Colfer
Conceptualization (equal), Data curation (equal), Formal analysis (lead), Investigation (lead), Methodology (equal), Resources (equal), Software (equal), Validation (equal), Visualization (lead), Writing – original draft (lead), Writing – review & editing (equal)

Michele Shelly Conroy 0009-0002-9426-2492
Data curation (equal), Formal analysis (equal), Investigation (equal), Methodology (equal), Resources (equal), Software (lead), Validation (equal), Visualization (equal), Writing – review & editing (equal)

Núria Bagués 0000-0002-9360-0915
Data curation (equal), Formal analysis (equal), Investigation (equal), Methodology (equal), Resources (equal), Validation (equal), Visualization (equal), Writing – review & editing (equal)

David McComb 0000-0003-3763-9652
Formal analysis (equal), Funding acquisition (equal), Investigation (equal), Methodology (equal), Project administration (equal), Resources (equal), Supervision (equal), Validation (equal), Writing – review & editing (equal)

Jonathan Alaria 0000-0001-5868-0318
Data curation (equal), Formal analysis (equal), Investigation (equal), Methodology (equal), Resources (equal), Software (lead), Supervision (equal), Validation (equal), Writing – review & editing (equal)

Michael Schmidt 0000-0002-5601-460X
Data curation (equal), Formal analysis (equal), Investigation (equal), Methodology (equal), Resources (equal), Validation (equal), Writing – review & editing (equal)

Roger W. Whatmore 0000-0001-9455-5848
Formal analysis (equal), Investigation (equal), Methodology (equal), Resources (equal), Software (lead), Supervision (equal), Validation (equal), Writing – review & editing (equal)

Lynette Keeney 0000-0003-0980-514X
Conceptualization (lead), Data curation (lead), Formal analysis (equal), Funding acquisition (lead), Investigation (equal), Methodology (equal), Project administration (lead), Resources (equal), Software (equal), Supervision (lead), Validation (lead), Visualization (equal), Writing – original draft (equal), Writing – review & editing (lead)

References

[1] Whyte J R and Gregg J M 2015 A diode for ferroelectric domain-wall motion *Nat. Commun.* **6** 7361
[2] Sharma P, Zhang Q, Sando D, Lei C H, Liu Y, Li J, Nagarajan V and Seidel J 2017 Nonvolatile ferroelectric domain wall memory *Sci. Adv.* **3** e1700512
[3] Sharma P *et al* 2019 Conformational domain wall switch *Adv. Funct. Mater.* **29** 1807523
[4] Gradauskaite E, Meisenheimer P, Müller M, Heron J and Trassin M 2021 Multiferroic heterostructures for spintronics *Phys. Sci. Rev.* **6** 20190072
[5] Spaldin N A and Ramesh R 2019 Advances in magnetoelectric multiferroics *Nat. Mater.* **18** 203–12
[6] Keeney L, Maity T, Schmidt M, Amann A, Deepak N, Petkov N, Roy S, Pemble M E and Whatmore R W 2013 Magnetic field-induced ferroelectric switching in multiferroic Aurivillius phase thin films at room temperature *J. Am. Ceram. Soc.* **96** 2339–57
[7] Faraz A, Maity T, Schmidt M, Deepak N, Roy S, Pemble M E, Whatmore R W and Keeney L 2017 Direct visualization of magnetic-field-induced magnetoelectric switching in multiferroic Aurivillius phase thin films *J. Am. Ceram. Soc.* **100** 975–87
[8] Halpin J, Schmidt M, Whatmore R W and Keeney L 2025 Impact of magnetic ion substitution on the crystal structure of multiferroic Aurivillius phases *APL Electron. Dev.* **1** 016104
[9] Ruddlesden S N and Popper P 1957 New compounds of the K_2NIF_4 type *Acta Crystallogr.* **10** 538–9
[10] Dion M, Ganne M and Tournoux M 1981 Nouvelles familles de phases $M^{I}M^{II}{}_2Nb_3O_{10}$ a feuillets "perovskites" *Mater. Res. Bull.* **16** 1429–35
[11] Jacobson A J, Lewandowski J T and Johnson J W 1986 Ion exchange of the layered perovskite $KCa_2Nb_3O_{10}$ by protons *J. Less-Common Met.* **116** 137–46
[12] Müller-buschbaum H 1989 The crystal chemistry of high-temperature oxide superconductors and materials with related structures *Angew. Chem. Int. Ed. Engl.* **28** 1472–93 [In German]
[13] Zurbuchen M A *et al* 2007 Morphology, structure, and nucleation of out-of-phase boundaries (OPBs) in epitaxial films of layered oxides *J. Mater. Res.* **22** 1439–71
[14] Deepak N, Carolan P, Keeney L, Pemble M and Whatmore R W 2015 Tunable nanoscale structural disorder in Aurivillius phase, n = 3 $Bi_4Ti_3O_{12}$ thin films and their role in the transformation to n = 4, $Bi_5Ti_3FeO_{15}$ phase *J. Mater. Chem. C* **3** 5727–32
[15] Zhang Y, Han M G, Sando D, Wu L, Valanoor N and Zhu Y 2021 Antiphase-boundary-engineered domain switching in a (110)-Oriented $BiFeO_3$ film *ACS Appl. Electron. Mater.* **3** 3226–33
[16] Wei X K, Tagantsev A K, Kvasov A, Roleder K, Jia C L and Setter N 2014 Ferroelectric translational antiphase boundaries in nonpolar materials *Nat. Commun.* **5** 3031
[17] Kim J *et al* 2021 Superconducting Sr_2RuO_4 thin films without out-of-phase boundaries by higher-order Ruddlesden–popper intergrowth *Nano Lett.* **21** 4185–92
[18] Nakajima H, Kurushima K, Mine S, Tsukasaki H, Matsuoka M, Gao B, Cheong S-W and Mori S 2021 Charged domain boundaries stabilized by translational symmetry breaking in the hybrid improper ferroelectric $Ca_{3-x}Sr_xTi_2O_7$ *Commun. Mater.* **2** 109
[19] Kumar A, Wetterskog E, Lewin E, Tai C-W, Akansel S, Husain S, Edvinsson T, Brucas R, Chaudhary S and Svedlindh P 2018 Effect of *in situ* electric-field-assisted growth on antiphase boundaries in epitaxial Fe_3O_4 thin films on MgO *Phys. Rev. Mater.* **2** 054407
[20] Ruiz-gómez S, Pérez L, Mascaraque A, Quesada A, Prieto P, Palacio I, Martín-garcía L, Foerster M, Aballe L and de la Figuera J 2018 Geometrically defined spin structures in ultrathin Fe_3O_4 with bulk like magnetic properties *Nanoscale* **10** 5566–73
[21] A Kelly and K Knowles (ed) 2012 Dislocations in Crystals *Crystallography and Crystal Defects* (Wiley) pp 269–304
[22] Keeney L, Saghi Z, O'sullivan M, Alaria J, Schmidt M and Colfer L 2020 Persistence of ferroelectricity close to unit-cell thickness in structurally disordered Aurivillius phases *Chem. Mater.* **32** 10511–23
[23] Yu X, Li Z, Bai Y, Zhang Q, Chen P, Zhao H, Gu L and Zhan Q 2026 Defect-driven polarization reconfiguration in Bi3.15Nd0.85Ti3O12 film *Scr. Mater.* **274** 117121
[24] Moore K, O'connell E N, Griffin S M, Downing C, Colfer L, Schmidt M, Nicolosi V, Bangert U, Keeney L and Conroy M 2022 Charged domain wall and polar vortex topologies in a room-temperature magnetoelectric multiferroic thin film *ACS Appl. Mater. Interfaces* **14** 5525–36
[25] Keeney L, Downing C, Schmidt M, Pemble M E, Nicolosi V and Whatmore R W 2017 Direct atomic scale determination of magnetic ion partition in a room temperature multiferroic material *Sci. Rep.* **7** 1737
[26] Pyatakov A P 2018 Magnetoelectricity goes local: from bulk multiferroic crystals to ferroelectricity localized on magnetic topological textures *Physica B* **542** 59–62
[27] Nataf G F, Guennou M, Gregg J M, Meier D, Hlinka J, Salje E K H and Kreisel J 2020 Domain-wall engineering and topological defects in ferroelectric and ferroelastic materials *Nat. Rev. Phys.* **2** 634–48
[28] Meier D and Selbach S M 2022 Ferroelectric domain walls for nanotechnology *Nat. Rev. Mater.* **7** 157–73
[29] Hong Z, Das S, Nelson C, Yadav A, Wu Y, Junquera J, Chen L-Q, Martin L W and Ramesh R 2021 Vortex domain walls in ferroelectrics *Nano Lett.* **21** 3533–9

[30] Gradauskaite E, Hunnestad K A, Meier Q N, Meier D and Trassin M 2022 Ferroelectric domain engineering using structural defect ordering *Chem. Mater.* **34** 6468–75
[31] Dorrian J F, Newnham R E, Smith D K and Kay M I 1972 Crystal structure of Bi4Ti3O12 *Ferroelectrics* **3** 17–27
[32] Frankl D R and Venables J A 1970 Nucleation on substrates from the vapour phase *Adv. Phys.* **19** 409–56
[33] Markov I and Stoyanov S 1987 Mechanisms of epitaxial growth *Contemp. Phys.* **28** 267–320
[34] Tung S K 1965 The effects of substrate orientation on epitaxial growth *J. Electrochem. Soc.* **112** 436
[35] Eckstein J N, Bozovic I, Schlom D G and Harris J S Jr 1990 Growth of untwinned $Bi_2Sr_2Ca_2Cu_3Ox$ thin films by atomically layered epitaxy *Appl. Phys. Lett.* **57** 1049–51
[36] Sando D 2022 Strain and orientation engineering in ABO_3 perovskite oxide thin films *J. Phys: Condens. Matter* **34** 153001
[37] García-guaderrama M, Fuentes-montero L, Rodriguez A and Fuentes L 2006 Structural characterization of Bi6Ti3Fe2O18 obtained by molten salt synthesis *Integr. Ferroelectr.* **83** 41–47
[38] Treacy M M J, Newsam J M and Deem M W 1991 A general recursion method for calculating diffracted intensities from crystals containing planar faults *Proc. R. Soc. Lond. Ser. A* **433** 499–520
[39] Whatmore R W, Dutta D and Keeney L 2025 A model for out-of-phase boundary induced x-ray diffraction peak profile changes in Aurivillius oxide thin films *J. Appl. Crystallogr.* **58** 1191–204
[40] Lomanova N A, Morozov M I, Ugolkov V L and Gusarov V V 2006 Properties of Aurivillius phases in the Bi4Ti3O12-$BiFeO_3$ system *Inorg. Mater.* **42** 189–95
[41] Deepak N, Zhang P F, Keeney L, Pemble M E and Whatmore R W 2013 Atomic vapor deposition of bismuth titanate thin films *J. Appl. Phys.* **113** 187207
[42] Mietschke M, Chekhonin P, Molin C, Gebhardt S, Fähler S, Nielsch K, Schultz L and Hühne R 2016 Influence of the polarization anisotropy on the electrocaloric effect in epitaxial PMN-PT thin films *J. Appl. Phys.* **120** 114102
[43] Chekhonin P, Mietschke M, Pohl D, Schmidt F, Fähler S, Skrotzki W, Nielsch K and Hühne R 2017 Effect of substrate miscut on the microstructure in epitaxial $Pb(Mg_{1/3}Nb_{2/3})O_3$-$PbTiO_3$ thin films *Mater. Charact.* **129** 234–41
[44] Theis C, Yeh J, Schlom D, Hawley M and Brown G 1998 The influence of vicinal $SrTiO_3$ surfaces on the growth and ferroelectric properties of epitaxial $Bi_4Ti_3O_{12}$ thin films *Mater. Sci. Eng. B* **56** 228–33
[45] Deepak N, Carolan P, Keeney L, Zhang P F, Pemble M E and Whatmore R W 2015 Bismuth self-limiting growth of ultrathin $BiFeO_3$ films *Chem. Mater.* **27** 6508–15
[46] Hervoches C H, Snedden A, Riggs R, Kilcoyne S H, Manuel P and Lightfoot P 2002 Structural behavior of the four-layer Aurivillius-phase ferroelectrics SrBi4Ti4O15 and Bi5Ti3FeO15 *J. Solid State Chem.* **164** 280–91
[47] Krzhizhanovskaya M, Filatov S, Gusarov V, Paufler P, Bubnova R, Morozov M and Meyer D C 2005 Aurivillius phases in the Bi4Ti3O12/$BiFeO_3$ system: thermal behaviour and crystal structure *Z. Anorg. Allg. Chem.* **631** 1603–8 [In German]
[48] Nečas D and Klapetek P 2012 Gwyddion: an open-source software for SPM data analysis *Open Phys.* **10** 181–8
[49] Keeney L, Colfer L, Dutta D, Schmidt M and Wei G 2023 What lies beneath? Investigations of atomic force microscopy-based nano-machining to reveal sub-surface ferroelectric domain configurations in ultrathin films *Microstructures* **3** 2023041
[50] Colfer L, Keeney L and Schmidt M 2022 Probing ferroelectric behavior in Sub-10 nm bismuth-rich Aurivillius films by piezoresponse force microscopy *Microsc. Microanal.* **28** 1396–406
[51] Batuk D, Batuk M, Filimonov D S, Zakharov K V, Volkova O S, Vasiliev A N, Tyablikov O A, Hadermann J and Abakumov A M 2017 Crystal structure, defects, magnetic and dielectric properties of the layered Bi3n+1Ti7Fe3n–3O9n+11 perovskite-anatase intergrowths *Inorg. Chem.* **56** 931–42
[52] Batuk D, Tsirlin A A, Filimonov D S, Zakharov K V, Volkova O S, Vasiliev A, Hadermann J and Abakumov A M 2016 Bi3n+1Ti7Fe3n–3O9n+11 homologous series: slicing perovskite structure with planar interfaces containing anatase-like chains *Inorg. Chem.* **55** 1245–57
[53] MacLaren I, Wang L Q, Schaffer B, Ramasse Q M, Craven A J, Selbach S M, Spaldin N A, Miao S, Kalantari K and Reaney I M 2013 Novel nanorod precipitate formation in neodymium and titanium codoped bismuth ferrite *Adv. Funct. Mater.* **23** 683–9
[54] MacLaren I, Wang L, Craven A J, Ramasse Q M, Schaffer B, Kalantari K and Reaney I M 2014 The atomic structure and chemistry of Fe-rich steps on antiphase boundaries in Ti-doped $Bi_{0.9}Nd_{0.15}FeO_3$ *APL Mater.* **2** 066106
[55] Smith D J and Hutchison J L 1983 Intergrowths and defect structures in $Bi_9Ti_3Fe_5O_{27}$ revealed by high-resolution electron microscopy *J. Microsc.* **129** 285–93
[56] Cao X, Liu Z, Dedon L R, Bell A J, Esat F, Wang Y, Yu P, Wang C and Jin P 2017 Epitaxial $Bi_9Ti_3Fe_5O_{27}$ thin films: a new type of layer-structure room-temperature multiferroic *J. Mater. Chem. C* **5** 7720–5
[57] Wang L Q, Schaffer B, MacLaren I, Miao S, Craven A J and Reaney I M 2012 Atomic scale structure and chemistry of anti-phase boundaries in (Bi0.85Nd0.15)(Fe0.9Ti0.1)O_3 ceramics *J. Phys.: Conf. Ser.* **371** 012036
[58] Li L, Cheng X, Jokisaari J R, Gao P, Britson J, Adamo C, Heikes C, Schlom D G, Chen L-Q and Pan X 2018 Defect-induced hedgehog polarization states in multiferroics *Phys. Rev. Lett.* **120** 137602
[59] Dutta D *et al* 2025 Enhancing vertical ferroelectric polarization using growth spirals. ChemRxiv.(This content is a preprint and has not been peer-reviewed) (https://doi.org/10.26434/chemrxiv-2025-982tj-v2)
[60] Vasudevan R K, Matsumoto Y, Cheng X, Imai A, Maruyama S, Xin H L, Okatan M B, Jesse S, Kalinin S V and Nagarajan V 2014 Deterministic arbitrary switching of polarization in a ferroelectric thin film *Nat. Commun.* **5** 4971
[61] Rodriguez B J, Callahan C, Kalinin S V and Proksch R 2007 Dual-frequency resonance-tracking atomic force microscopy *Nanotechnology* **18** 475504
[62] Watanabe T and Funakubo H 2006 Controlled crystal growth of layered-perovskite thin films as an approach to study their basic properties *J. Appl. Phys.* **100** 051602
[63] Li Y L, Chen L Q, Asayama G, Schlom D G, Zurbuchen M A and Streiffer S K 2004 Ferroelectric domain structures in SrBi2Nb2O9 epitaxial thin films: electron microscopy and phase-field simulations *J. Appl. Phys.* **95** 6332–40
[64] Balke N, Choudhury S, Jesse S, Huijben M, Chu Y H, Baddorf A P, Chen L Q, Ramesh R and Kalinin S V 2009 Deterministic control of ferroelastic switching in multiferroic materials *Nat. Nanotechnol.* **4** 868–75